



Full length article



Mechanistic insights into hydration-driven shape memory response in keratinous avian feather structures

Phani Saketh Dasika^a, Yunlan Zhang^{a,1}, Tarah N. Sullivan^b, Sheron Tavares^b,
Marc A. Meyers^b, Pablo D. Zavattieri^{a,*}

^a Lyles School of Civil and Construction Engineering, Purdue University, West Lafayette, IN 47907, USA

^b Departments of Nanoengineering and Mechanical and Aerospace Engineering, Materials Science and Engineering Program, University of California San Diego, La Jolla, CA 92093, USA

ARTICLE INFO

Keywords:

Shape memory
Hydration-driven mechanisms
Avian feathers
Biomimetics

ABSTRACT

Keratinous materials found in the feather shafts of flying birds possess impressive mechanical attributes, combining excellent strength-to-weight balance, toughness, and more. In this study, we investigate the shape memory effect in bird feather shafts, examining its underlying design principles as templates for bioinspired shape memory composites. Through analytical and computational analysis, we aim to uncover the underlying rules and design guidelines based on stimulus-induced softening (pertaining to strength and/or stiffness) and swelling (pertaining to expansion in volume). More specifically, we study a one-dimensional case to examine the synergistic relationship between the matrix and fibers inside the feather structure. We propose three distinct micro-mechanical modeling approaches to evaluate the contribution of each hydration-induced effect—softening, swelling, and the combined action of both. In all models, the matrix is considered to be an elastic-perfectly plastic material that is sensitive to hydration, while the fibers are treated as purely elastic and unaffected by hydration. The findings of the study provide informative insights into the nuanced nature of swelling within the material, highlighting that its desirability is dependent on specific conditions and circumstances. Furthermore, we find that the softening component plays a large pivotal role in driving the process of shape recovery. Using the proposed analytical framework and design principles, we develop a conceptual feather shaft-like composite, followed by demonstrating its tunability in degree of shape recovery and its versatility in selecting constituent base material components. This research offers valuable core framework for exploring and designing advanced bioinspired shape memory materials while eliminating the need for traditionally active shape memory components, holding promising potential for actuation, deployment, and morphing purposes.

Statement of significance: This study investigates the shape-memory effect in bird feather shafts, offering bioinspired strategies for designing advanced shape-memory composites. Unlike conventional materials, which often rely on external stimuli or active components, our research focuses on hydration-driven mechanisms—specifically, matrix softening and swelling. Through micro-mechanical modeling, we demonstrate that softening is the key driver of shape recovery, while swelling plays a secondary role under specific conditions. These insights provide new, passive design principles for creating tunable shape-memory composites without the need for traditional active components. The findings have broad implications for applications in actuation, morphing, and reconfigurable systems, where material adaptability is crucial.

1. Introduction

The escalating complexity of engineering applications [1–4] has prompted the exploration of advanced materials capable of providing superior performance and the incorporation of these materials into

intelligent devices [5,6]. Among the various types of materials that have received considerable attention across different fields, stimuli-responsive materials are notable for their capability to exhibit swift reactions to external stimuli and their versatility in applications [7–14]. In particular, a subgroup called shape memory materials

* Corresponding author.

E-mail address: zavattie@purdue.edu (P.D. Zavattieri).

¹ Present address: Civil, Architectural and Environmental Engineering, University of Texas, Austin, USA.

<https://doi.org/10.1016/j.actbio.2025.02.017>

Received 8 October 2024; Received in revised form 15 January 2025; Accepted 6 February 2025

Available online 7 February 2025

1742-7061/© 2025 Acta Materialia Inc. Published by Elsevier Inc. All rights reserved, including those for text and data mining, AI training, and similar technologies.

(SMMs) exhibits shape memory effect (SME), a special property that enables them to recover their original “memorized” shape [15] after being severely deformed or quasi-plastically distorted [16] when triggered by external stimuli like heat [17], light [18], electricity [19], magnetic fields [20] or simply water [21].

The two most common types of SMMs are shape memory alloys (SMAs) and shape memory polymers (SMPs). SMAs achieve the shape memory effect (SME) by undergoing thermoelastic martensitic-to-austenitic phase transformations [22]. Alternately, SMPs attain SME through a combination of polymer morphology [23] and a dual-segment (elastic-to-transition) system [24]. SMAs and SMPs have demonstrated superior properties in their ability to undergo reversible deformation and shape recovery, hence finding their advantageous characteristics in various applications, including MEMS [25,26], actuators [27,28], aerospace [29,30], and medical devices [31,32]. Nevertheless, these materials still face certain challenges and limitations despite their promising characteristics. For instance, SMAs are associated with high costs [33], often require complex and energy-intensive manufacturing processes [34], and have limited customization options [1]. Meanwhile, SMPs are associated with developmental challenges requiring high levels of experience and expertise in the field of polymers along with significant trial periods [1] and may yet suffer from limited mechanical strength and durability. Huang et al. (2010) [16] introduced shape memory hybrids that resemble SMPs in their elastic-to-transition segment system while aiming to provide a broader range of customizable functions and features for engineering applications; however, research in this field is still ongoing and remains relatively understudied. Recently, studies have been conducted on developing SMMs utilizing architected materials [35] and 4D printing techniques [36]. Despite the advancements in SMM research and the exploration of modern materials and manufacturing techniques, there is still much to be uncovered and understood in this dynamic field.

Nature offers a valuable perspective on shape memory and emulating these mechanisms has the potential to overcome challenges faced by traditional SMMs. Specifically, the mechanism found in keratinous materials within the feather shafts of birds has emerged as a

scientifically compelling area of study. By investigating the distinctive structural and functional properties of these natural materials, we aim to uncover new insights and develop engineering design guidelines to address the existing gaps in research. Feathers exhibit exceptional structural resilience with a diaphanous structure, enabling them to withstand the stresses and strains of flight, which include aerodynamic loading, impacts near structures during takeoff and landing, and bending due to maneuverability [37]. Regular grooming is, therefore, vital for birds to maintain the structural integrity of their feathers. It helps prevent damage caused by flight and deterioration from ectoparasites, such as feather mites and feather-degrading bacteria [38–40], which can increase friction between feathers and contribute to wear, as well as damage from surface contact. Previous research has indicated that birds use grooming methods such as preening, scratching, sunning, dusting, anointing, and frequent bathing to protect themselves against these ectoparasites [41,42]. However, recent research has unveiled that the hydration stages from frequent bathing bouts also aid in recovering the shape and strength of feather shafts by repairing fractured sections and reversing the plastic deformation incurred by predatory attacks, excessive use, or other unforeseen calamities [43–45]. Given that feathers usually undergo replacement only once a year, such recuperation of the feather shaft is critical for the survival of birds [46].

To better understand the mechanism underlying the SME exhibited by feather shafts, it is important to conduct a thorough investigation into the intricate internal architecture of these structures at the micro- and nanoscales. Feather shafts comprise two distinct sections, the rachis and the calamus, where the former is a rectangular, foam-filled structure formed by medullary cells, and the latter is an elliptical, hollow implant that anchors the feather into the skin of the bird [47] (see Fig. 1). The key player in both sections is β -keratin, a biopolymer composite made of a hierarchical arrangement of fibers produced by keratinous cells and is essentially “dead tissue” [48]. In Fig. 1, the hierarchical structure of feather shafts is determined based on the size and organization of the components. At the sub-nanoscale, the crystalline filaments of β -keratin, with a diameter of approximately 3 nm (see Fig. 1), are intertwined among amorphous matrix proteins. This intricate filament-matrix

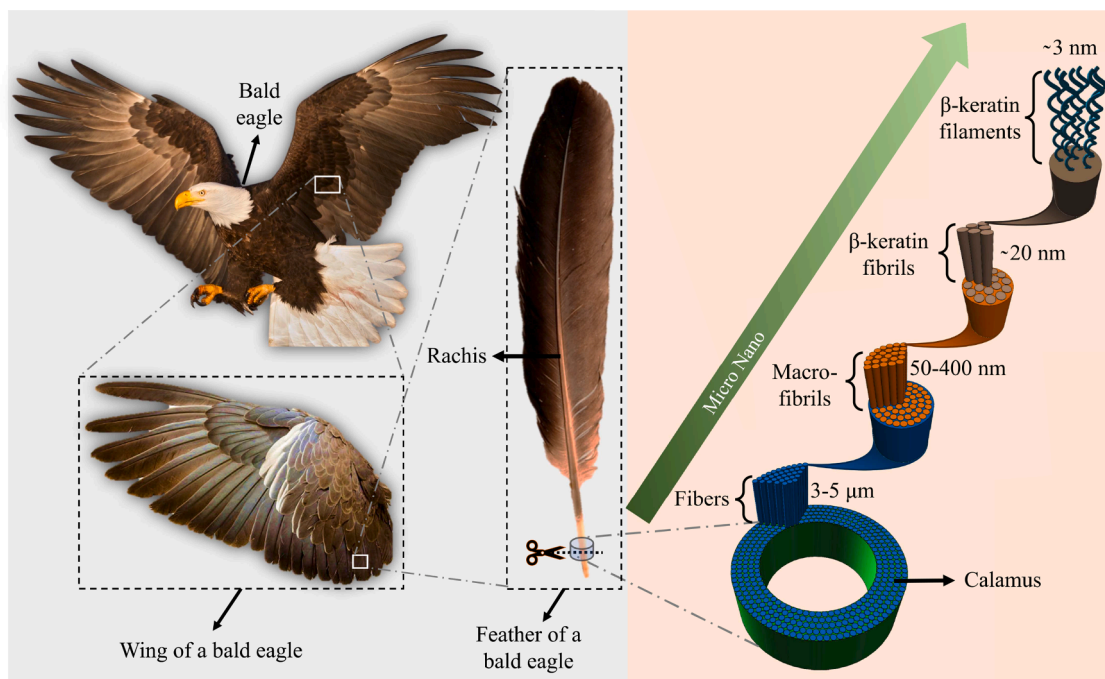


Fig. 1. Hierarchical Structure of Feather Shafts. (a) Illustration of the multilevel architecture in a bald eagle with (b) a schematic diagram detailing the internal micro- and nano-structures across the cross-section of the calamus region within the feather shaft. This cross-section reveals the intricate arrangement of the fibers, macro-fibrils, β -keratin fibrils, and β -keratin filaments, elucidating the complex architectures that are responsible for the impressive SME properties observed in bird feathers. (The raw images for (a) were taken from <https://www.freepik.com/> and edited further by the authors).

composite forms macro-fibrils with a diameter of around 200 nm, surrounded by amorphous inter-macro-fibrillar material. These macro-fibrils merge to form fibers measuring 3–5 μm in diameter, resulting in the development of well-organized lamellae within the thick exterior of the feather shaft [48–53].

The existing literature reports that feathers [43–45], along with other keratinous materials such as pangolin scales [54], sheep horns [55], and animal hair [56], can manifest shape memory behavior upon being hydrated, analogous to other natural substances like chitosan [57] and spider silk [58]. Xiao et al. (2017) [56] demonstrated that camel hair could exhibit shape memory not only through hydration, but also through exposure to heat, redox agents, and UV light. Huang et al. (2019) [55] attributed the shape recovery process in the Bighorn sheep horn to water infiltration of the amorphous keratin matrix, leading to swelling and subsequent breaking and reforming of hydrogen bonds, allowing the deformed crystalline regions of the intermediate keratin filaments to regain their original shape. Liu et al. (2016) [54] observed significant hydration-assisted shape recovery (up to 98 %) in compressed peacock tail feathers, which they attributed to viscoelasticity relaxation, swelling effect, and water-induced structural changes. Sullivan et al. (2018) [45] extended the study by subjecting feathers to cyclic loading in real-world conditions to investigate the flexural and failure behavior of the shaft, finding that the recovery of shape and strength is associated with the swelling of the matrix and subsequent straightening of fibers within the β -keratinous nanocomposite structure. A steel wool-reinforced cellulose sponge was used to show the impact of swelling, with the cellulose sponge swelling significantly with hydration, while the steel wool fibers did not. Despite the widely accepted notion that the shape memory effect of keratinous materials results from hydrogen bond breakage and water-induced swelling [59], the exact mechanism responsible for this phenomenon has yet to be well ascertained [60].

Based on recent literature [45,61], the prevailing mechanism proposed for recovering shape and strength in feathers can be summarized as follows. See Fig. 2 for an illustration depicting the feather shape memory process on a simplified representative element (SRE). In addition to the theoretical framework illustrated in Fig. 2a, the Scanning Electron Microscopy (SEM) images presented in Fig. 2b provide necessary experimental validation of the proposed shape memory mechanism across multiple length scales [45]. These images capture the intricate microstructural changes occurring within the middle rachis section of a *Cape Vulture* (*G. coprotheres*) feather, visualizing key stages of the shape recovery process. The recovery cycle starts with the initial configuration characterized by a layered nanocomposite structure of partially crystalline intermediate β -keratin filaments embedded in an amorphous matrix within the feather cortex strip, initially stress-free (see Fig. 2a at t_1). The fibers are depicted as darker strips, separated by the matrix, with the spacing between fibers represented as d_0 . This initial configuration is also captured in Fig. 2b at t_1 , where SEM images reveal the pristine arrangement of the keratin filaments and matrix at three magnification levels, confirming the unstrained architecture of the feather structure. These unstrained SEM images offer a detailed look at the hierarchical organization, serving as a visual reference for the subsequent stages of mechanical deformation and hydration recovery. When the feather undergoes flexural bending, Euler buckling (in compression) of these intermediate filaments below the neutral axis is triggered, which is effectively accommodated by the inelastic response of the amorphous matrix, ultimately resulting in the deformation of the feather (see Fig. 2a at t_2). The SEM images at t_2 in Fig. 2b reveal clear signs of filament buckling and matrix plastic deformation. At higher magnification, localized deformation zones are visible, supporting the theoretical model where the matrix absorbs inelastic strain and the keratin fibers store elastic energy. During hydration, water molecules selectively infiltrate the amorphous matrix, leading to significant softening and inelastic deformation. This is accompanied by swelling, as indicated by an increase in spacing from d_0 to d_1 (see Fig. 2a at t_3). The rigid filaments

remain unaltered but store elastic energy due to buckling. This combination of matrix softening, swelling, and elastic energy accumulation promotes the stretching and initial straightening of the feather shaft. Subsequent matrix swelling allows for increased spacing (up to d_2) between the matrix and fibers, facilitating complete reorientation of the fibers (see Fig. 2a at t_4). SEM images of the hydrated configuration (see Fig. 2b at t_4) showcase the effects of water infiltration, with the matrix visibly swollen and the spacing between the fibers increased. This reorientation is accompanied by reverse plastic flow within the matrix and an associated increase in the radius of curvature of the feather shaft from R_1 to R_2 . The magnified SEM images at t_4 further reveal the smoother texture of the hydrated matrix compared to the rougher, compressed appearance observed in the deformed state, visually confirming the plastic flow and recovery of the matrix. The final phase of the shape recovery cycle is dehydration, whereby the surplus water molecules are extracted from the amorphous matrix, causing it to contract to the initial spacing (d_0) without inducing further inelastic deformation, thus restoring the feather to its initial configuration (see Fig. 2a at t_5).

While the SEM images above are provided for the *Cape Vulture* (*Gyps coprotheres*), this is not the only bird species to exhibit such shape memory properties. Many birds, including common species encountered in daily life, demonstrate shape memory behavior in their feathers. As a quick example, we tested the same shape memory behavior on a crow (*Corvus brachyrhynchos*) and observed similar results. In our experiments, we initially deformed the feather and subsequently allowed it to recover its structural shape by hydrating it in water under conditions analogous to those used in the previous experiments described in [45]. The crow feather showed almost complete recovery, as anticipated. Additional information on the crow feather experiments, including experimental images with optical microscopy close-ups (Fig. S2) and a video demonstrating the recovery process, can be found in the supplementary materials.

In this study, we examine this prevailing mechanism by meticulously investigating the individual impacts of softening and swelling and then subsequently analyzing the combined effect of these phenomena occurring concurrently within the amorphous matrix. To achieve this task, we constructed three micro-mechanical (MM) models and utilized these to study the impact of hydration-induced changes through analytical equations and finite element analysis (FEA). Rather than attempting to experimentally validate the models, our approach is rooted in extensive mathematical analysis informed by experimental studies from the literature that have documented the shape memory behavior of feathers. Building on this mathematical framework and design principles, we developed and studied what we will call a conceptual feather shaft-like composite (CFSC) that aims to emulate the natural functioning of the inelastic amorphous matrix flow and resilient keratin fibrils observed in the calamus section of bird feather shafts. Our goal is to leverage this knowledge seen in nature to use as blueprints to design shape memory materials with enhanced mechanical performance with a provision for high versatility in manufacturability by eliminating the need for active shape memory components.

The rest of the paper reads as follows—we begin by examining the shape memory effect in feather shafts, focusing on the necessary material properties and the interactions between the amorphous matrix and the resilient fibers. Following that, we conduct an analytical analysis of three MM models, allowing us to investigate the individual impacts of softening and swelling, as well as their combined effects on shape memory behavior. We then move on to the development of computational benchmarking models, which play a crucial role in testing and validating our findings. In the subsequent section, we illustrate the potential of the CFSC in terms of tunability and versatility, emphasizing its adaptability for use in various applications across different fields. Finally, we conclude with discussions, summarizing our findings, and provide insights into potential future research directions.

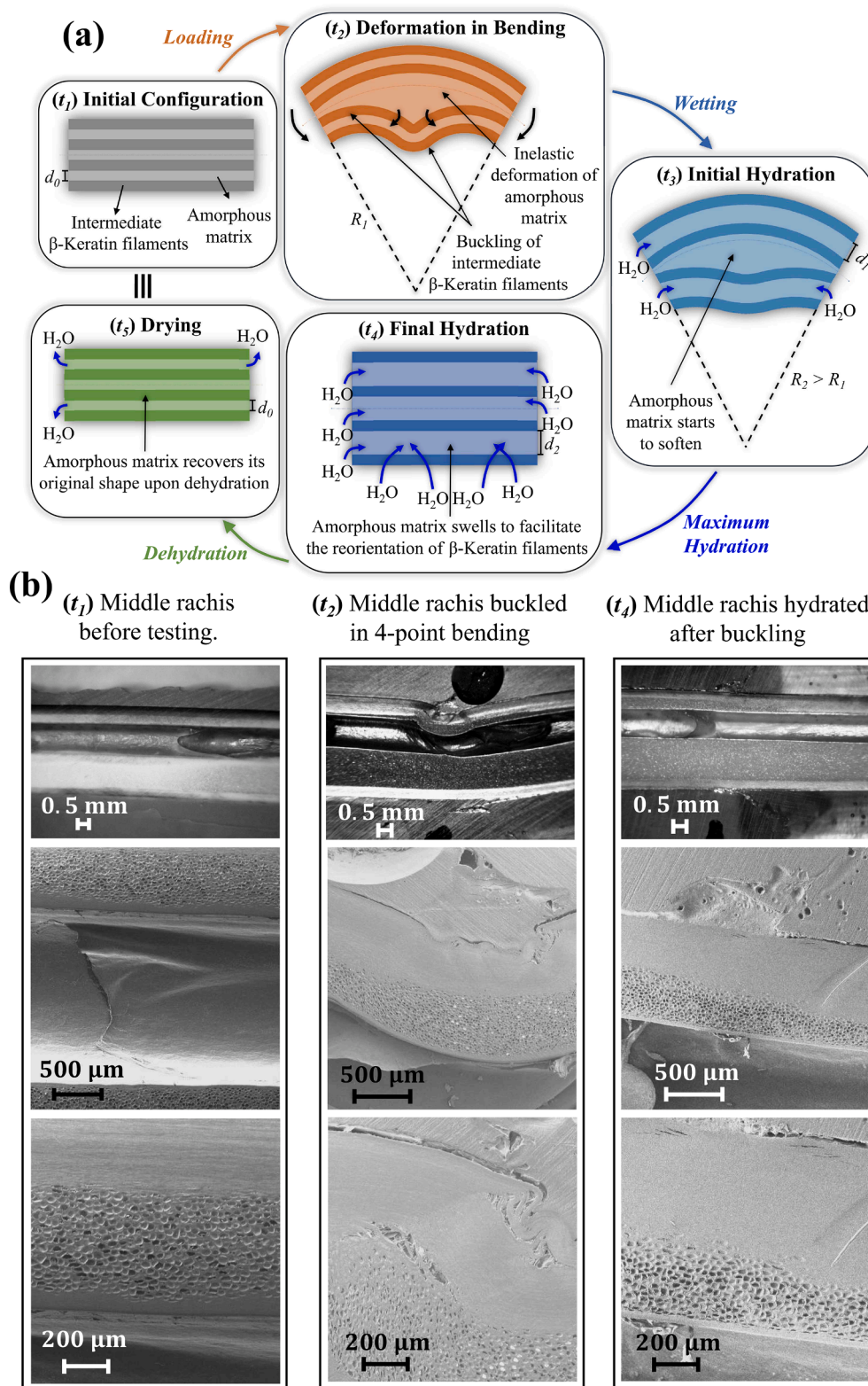


Fig. 2. Shape Recovery Process in Feather Shafts: (a) Current Postulation of shape recovery; (t₁) The process begins with the simplified representative element (SRE) of the feather shaft in its initial configuration, showing the β -keratin filaments embedded in an amorphous matrix with an internal spacing of d_0 . (t₂) The SRE is subjected to flexural bending, causing the amorphous matrix to deform inelastically and the β -keratin filaments to buckle under compression. (t₃) To initiate the shape recovery, the SRE is subjected to hydration, wherein the water molecules selectively permeate into the amorphous matrix, causing it to soften, while fibers remain unaffected except for an increase in their internal spacing to d_1 due to swelling of the matrix. (t₄) The matrix fully swells to a spacing of d_2 , allowing the β -keratin filaments to straighten out completely. (t₅) SRE is allowed to dry to remove excess water molecules, and it retains the recovered shape, which is geometrically equivalent to its initial configuration. (b) SEM images are shown for various length scales of feathers at (t₁) initial configuration, (t₂) deformed configuration, and (t₄) hydrated configuration of the middle rachis section of a *Cape Vulture* (*G. coprotheres*) feather. At each configuration, SEM images are provided at three magnification levels, with scale bars provided. (Images for (a) are designed based on the concept from [45] and (b) is adapted with permission from [45]).

2. Decoding shape memory effect in feather shafts: modeling of matrix-fiber synergistic interaction

The ability of the analytical feather shaft model to manifest SME stems from harnessing the synergistic behavior of the matrix-fiber constituents, operating under assumptions regarding the individual material properties. The primary framework utilized in constructing this model is based on a simple one-dimensional (1D) MM slab model where the matrix and fibers are assumed to have a perfect bond. The proportion of each constituent in the MM model can be quantified by the respective volumes occupied by the matrix (V_M) and fibers (V_F). The central objective is to investigate the fundamental factors responsible for SME by focusing on the minimum essential characteristics of the matrix and fibers that contribute to shape memory. In line with the 1D assumption, we focus on uniaxial stress, intentionally excluding consideration of transversal strains. This simplified 1D approach serves as our starting point, as it allows us to investigate the fundamental aspects of shape memory effects. By narrowing our focus to uniaxial stress, we aim to achieve a more precise and focused understanding of the underlying SME phenomena. Following recent literature [45], the matrix is modeled as an elastic-perfectly plastic material with two distinct regimes: a purely elastic regime characterized by Young’s modulus E_M^D in its dry state, followed by an instantaneous transition to a strictly plastic regime once the yield stress σ_y^D is reached. Upon hydration, the matrix experiences a reduction in its Young’s modulus to E_M^H (lower than E_M^D) and a reduction in yield stress to σ_y^H (lower than σ_y^D), as shown in Fig. 3. This behavior parallels the compliant amorphous matrix observed in keratinous materials [45,62–64], where in the dry state, densely packed

polymer chains provide rigidity through strong interchain interactions, and upon hydration, water molecules selectively interact with the amorphous matrix, acting as cross-links between chains, thereby reducing these interchain interaction [62] and resulting in softening. The significant reduction in stiffness and flow stress of the hydrated matrix enhances the effectiveness of the restorative forces exerted by the fibers. Additionally, the matrix may experience volumetric expansion (swelling) as water occupies voids within the disordered regions. Here, we use an analytical approach to examine the role of swelling in the matrix during the hydration stage.

On the other hand, the fibers are assumed to be unaffected by hydration [65] and do not undergo plastic deformation, thus maintaining a constant Young’s modulus E_F as shown in Fig. 3. This characteristic allows them to retain their elasticity throughout, resembling the tough crystalline intermediate filaments observed in keratinous materials [45, 62–64]. Consequently, these elastic fibers play a significant role in the restorative shape recovery mechanism by operating as restitutive springs. This is akin to the highly ordered dense structure of crystalline filament regions in a feather cortex that provides greater stiffness compared to the amorphous matrix in a feather cortex. To further elucidate the unaffected swelling behavior of the fibers feather shafts, additional visual evidence is presented in Fig. S1. These images, comparing the dry and hydrated states, demonstrate that even with up to 80 % water uptake due to hydration, the dimensional changes are minimal, with the longitudinal (length) dimension showing little to no change, while the lateral dimensions increasing by less than 10 % (see Fig. S1a). This anisotropic swelling behavior is driven by the arrangement of longitudinal and circumferential fibers within the shaft. The

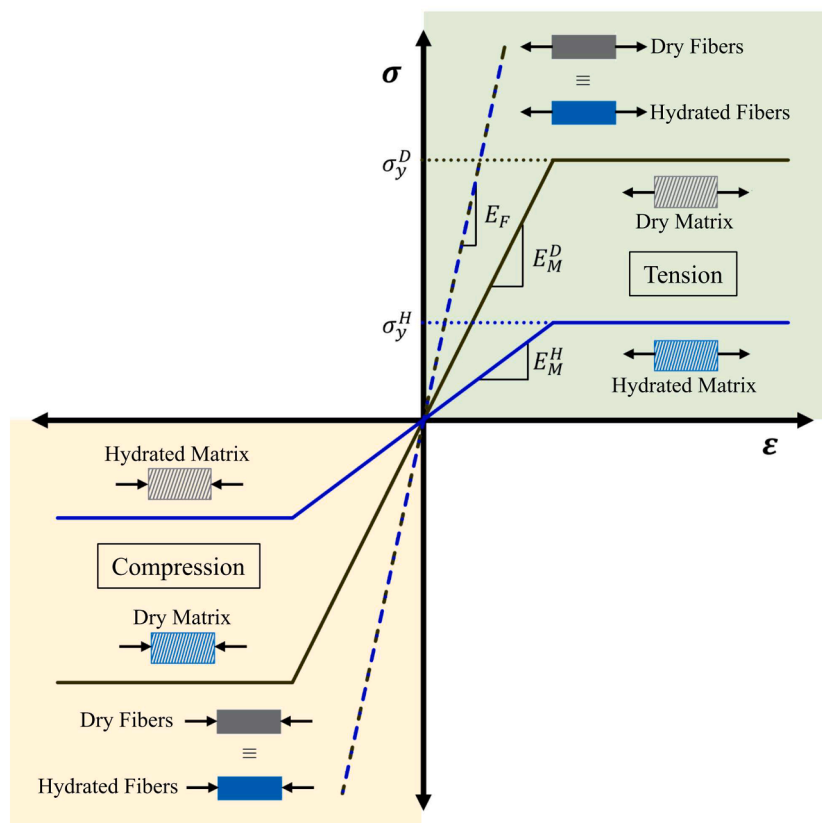


Fig. 3. Stress-strain ($\sigma - \epsilon$) response of matrix and fibers in both dry and hydrated states under tension and compression. The matrix in its dry state (solid grey) behaves as an elastic-perfectly plastic material with Young’s modulus, E_M^D and yield stress, σ_y^D , respectively. When hydrated (solid blue), the Young’s modulus and yield stress are reduced to E_M^H ($< E_M^D$) and σ_y^H ($< \sigma_y^D$), respectively, while still behaving as an elastic-perfectly plastic matrix. The fibers are always linearly elastic, unaffected by hydration (hyphenated brown and blue), and are stiffer than the matrix with Young’s modulus of E_F ($> E_M^D$). Both the matrix and fibers have symmetric mechanical behavior under tension and compression.

circumferential fibers limit diametral expansion, while the observed areal increase is attributed to swelling perpendicular to the fibers (see Fig. S1b).

In the schematic shown in Fig. 3, it is important to note that the yield strain values for the dry and hydrated states need not be the same. The schematic is intended to illustrate general trends rather than specific values, as the yield strain depends on the relative changes in Young’s modulus and yield stress upon hydration. However, this variation does not affect the conclusions of this study.

Building on these underlying assumptions and principles, we have formulated three distinct MM models to analytically examine and analyze the individual and combined influences of softening and swelling in the hydration-dependent elastic-perfectly plastic matrix. The fibers are considered resilient and impervious to hydration in all models, exhibiting purely elastic behavior. However, the effects of hydration on the matrix within these MM models are defined as follows:

- MM model-1 (Softening only): Upon hydration, the matrix experiences a significant decrease in both Young’s modulus and yield stress, leading to substantial softening. This model focuses exclusively on the mechanical changes of the matrix, disregarding any swelling.
- MM model-2 (Swelling only): Upon hydration, the matrix experiences swelling which pertains to volumetric expansion, while the mechanical properties, such as stiffness and strength, remain unaltered.
- MM model-3 (Softening and Swelling): Upon hydration, the matrix experiences both softening and swelling simultaneously.

In the following sections, we will explore each of these MM models individually. Note that in the case of a MM model where neither swelling nor softening occurs, the matrix, once plastically deformed, will remain in this deformed configuration, exhibiting no shape memory behavior.

2.1. MM model-1 (Softening only)

The 1D MM model, illustrated in Fig. 4a, is fixed on its left edge, and a uniaxial tensile testing scenario is investigated under displacement-controlled loading. Initially, at time t_1 , the stress-free model is characterized by zero strain (ϵ_1) with the positions of the fibers and matrix marked at the origin in the schematic graphs shown in Fig. 4(b and c). Subsequently, the composite is subjected to tensile loading (under uniaxial stress conditions), resulting in an elongation Δ_M until it reaches a strain value of $\epsilon_2 (= \Delta_M / L_0)$ at t_2 . The fiber component exhibits a purely linear elastic response, represented by the path marked as I_F from configurations at time t_1 to t_2 , as shown in Fig. 4c (the dashed red curved line with an arrow indicates the initial and end state. The stress-strain curve of the fiber remains elastic following the blue dashed straight line). In contrast, the matrix component initially exhibits elastic behavior until reaching the yield stress (σ_y^D), beyond which it deforms plastically represented by path I_M from configurations at time t_1 to t_2 , as shown in Fig. 4b (all paths are schematic directional indications and are depicted by dashed red lines). The strain in the model at time t_2 can be determined analytically using the equation $\epsilon_2 = (\Delta_M / L_0)$, where Δ_M denotes the change in length resulting from the stretching elongation, and L_0 denotes the initial length of the model (see Fig. 4a).

In the subsequent step of unloading, represented by paths II_M and II_F in Fig. 4(b and c) from configurations at time t_2 to t_3 , the applied tensile load is removed. This causes a reduction in the strain of the model because of spring-back (see Fig. 4a), leading to reach a strain value of ϵ_3 . At time t_3 , while the elastic fibers experience tension as they attempt to return to their undeformed, zero-strain configuration, the matrix undergoes plastic deformation and enters a compressed state in equilibrium. In the absence of external forces and applying equilibrium, the zero-stress strain in the model at time t_3 can be determined using the following equation:

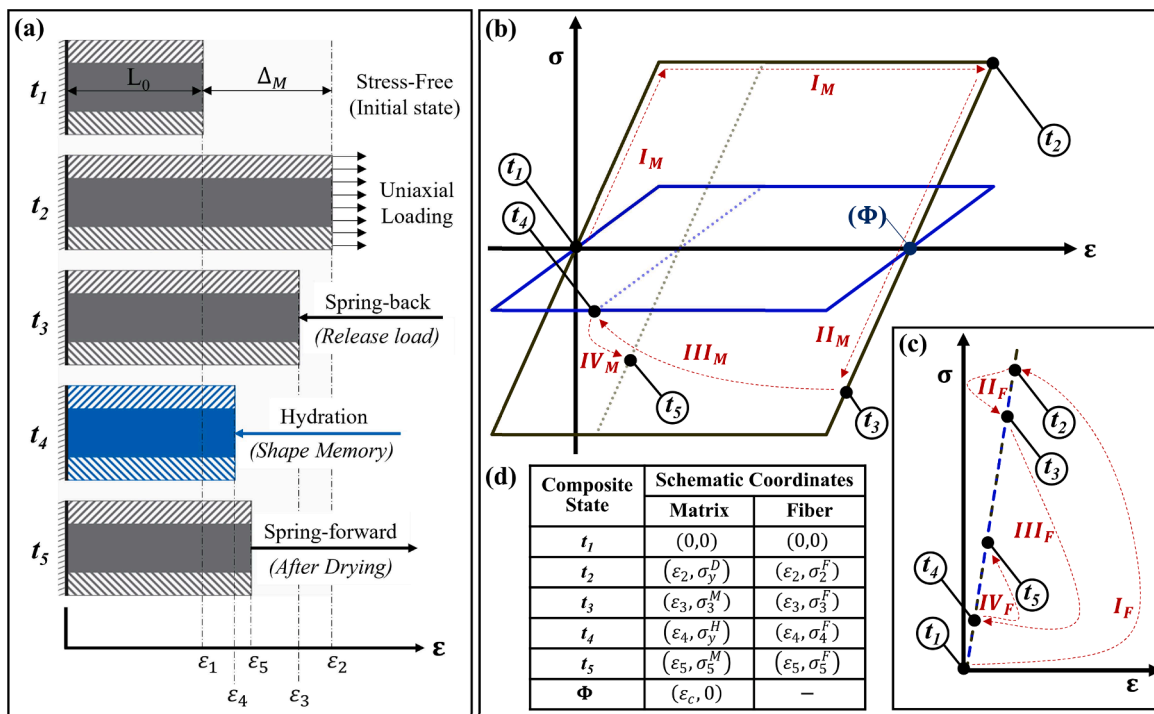


Fig. 4. Analysis of the MM Model-1 under Uniaxial Tensile Loading and Hydration. (a) Outline of the steps involved in the uniaxial tensile loading of the model followed by hydration and finally dehydration. Here, t_i represents the time steps at each significant configuration of the model during the test analysis. Roman numerals ($I - IV$) indicate the representative paths taken by the matrix and fibers during different stages: I - loading, II - unloading, III - hydration, and IV - dehydration, with these paths shown as hyphenated red lines. (b) Schematic stress-strain behavior in the dry (brown) and hydrated (blue) states of the matrix and (c) fiber. Representative paths are shown as hyphenated red lines. (d) Stress-strain coordinates of the matrix and fiber at significant time steps during the test.

$$\epsilon_3 = \frac{E_M^D V_M \epsilon_c}{E_M^D V_M + E_F V_F} \quad (1)$$

Here, ϵ_c indicates the persistent plastic deformation only within the matrix (i.e., if the matrix was considered to be isolated from the fibers). It measures the strain corresponding to the zero-residual stress at permanent deformation in the matrix, shown in Fig. 4(b and d) at point (Φ) and is given by the equation:

$$\epsilon_c = \frac{\Delta_M}{L_0} - \frac{\sigma_y^D}{E_M^D} \quad (2)$$

At this point in the study, the model has achieved a condition of equilibrium known as the *deformed* stage, indicated by a strain value of ϵ_3 . The persistent deformation, at ϵ_c , is caused purely inside the matrix and is not reliant on the elastic behavior of the fibers. This value is needed for understanding shape memory materials since it establishes the minimum deformation that must be overcome to return the material to its pre-programmed or original shape. Evidently, the applied deformation Δ_M impacts the values of ϵ_c and ϵ_3 , and the amount may change depending on the application.

To initiate the stage of shape recovery, the model is subjected to a hydration process. During this process, water is selectively permeated into the matrix, resulting in a substantial reduction in Young's modulus and yield stress of the matrix (path III_M in Fig. 4b), to E_M^H and σ_y^H , respectively. Conversely, the fibers remain impervious to hydration and serve as restitutive springs, aiding in the shape recovery (path III_F in Fig. 4c) of the MM model-1. This hydration-induced transition prompts a configuration shift in the composite from time t_3 to t_4 , leading to the attainment of a strain value of ϵ_4 , as depicted in Fig. 4a. The strain at t_4 is given by:

$$\epsilon_4 = \frac{V_M \sigma_y^H}{E_F V_F} \quad (3)$$

It is important to note that the hydration process, which acts as a temporary external stimulus, ends at some point, and the MM model-1 returns to its dry condition. As the model begins to lose moisture, it undergoes a series of adjustments. The fibers, acting as resilient springs, retain their original properties and remain unaffected by dehydration. Meanwhile, the matrix, which experienced reduced Young's modulus and yield stress during hydration, returns to its dry state characteristics. During this process, the MM model-1 exhibits a spring-forward behavior via paths IV_M and IV_F shown in Fig. 4(b and c) from time t_4 to t_5 until the strain reaches a value of ϵ_5 (Fig. 4a), which is given by:

$$\epsilon_5 = \frac{E_M^D V_M \epsilon'_c}{E_M^D V_M + E_F V_F} \quad (4)$$

Notably, the matrix is elastic with plastic strain at ϵ'_c in its final state, as given by:

$$\epsilon'_c = \frac{\sigma_y^H + E_M^H \epsilon_4}{E_M^H} \quad (5)$$

By closely observing the routes ($I - IV$) that the MM model-1 follows during its transitions between various configurations from times t_1 to t_5 , we gain a comprehensive understanding of its mechanical behavior encompassing loading, unloading, deformation, hydration, and dehydration stages. This detailed analysis provides crucial insights into the response of the model to external stimuli and its ability to exhibit shape memory behavior while emphasizing the significance of persistent plastic deformation in the matrix to achieve a *deformed* equilibrium state in the model. To validate the effectiveness of the model, we introduce the recovery strain parameter ($\epsilon_r = (\epsilon_3 - \epsilon_5)/\epsilon_3$) as a quantitative measure of the degree of shape recovery and is defined as:

$$\epsilon_r = 1 - \frac{\epsilon'_c}{\epsilon_c} \quad (6)$$

$$\Rightarrow \epsilon_r = 1 - \frac{\left(\frac{\sigma_y^H}{E_M^H}\right) + \left(\frac{\sigma_y^H V_M}{E_F V_F}\right)}{\left(\frac{\Delta_M}{L_0}\right) - \left(\frac{\sigma_y^D}{E_M^D}\right)} \quad (7)$$

This definition of shape recovery essentially serves as a crucial metric to assess the shape memory capabilities inherent in the composite material under study. While the model application and example presented in Fig. 4 are under uniaxial tensile stress conditions, it is essential to highlight that the same set of equations and principles can be readily applied to compression scenarios. Whether under tension or compression, the results derived from Eqs. (1)–(7) consistently yield the exact amount of recovery. This observation highlights a fundamental aspect of the shape memory and recovery process—its independence from the directionality of the applied load. This holds true within the context of our 1D model designed for a uniaxial composite under stress conditions.

2.2. MM model-2 (Swelling only)

While our evaluation here is limited to isolating the effect of swelling (by removing the softening of mechanical properties) on the shape memory properties within a uniaxial loading scenario, it is important to recognize that the natural occurrence of swelling in biological systems is considerably more intricate. The inherent complexities in multi-axial loading, such as bending and twisting, prevalent in natural scenarios with feathers, may introduce three-dimensional deformation and damage mechanisms where swelling could potentially play a significant and beneficial role. Our focused examination aims to elucidate the isolated impact of swelling on shape memory properties under uniaxial loading. While our model simplifies the scenario, it sets the stage for a deeper understanding of the interplay between swelling and mechanical behavior in bioinspired materials, offering a valuable foundation for future explorations into more complex loading scenarios.

Continuing our investigation, the matrix is now thought to solely experience swelling when subjected to hydration, and the identical tensile testing case as the model presented above is investigated. The stress and strain values of the MM model-2 and MM model-1 are identical during the initial stages (t_1 to t_3) because the hydration-dependent mechanisms of softening and swelling are not yet active. Additionally, it holds that $E_M^D \approx E_M^H \approx E_M$ and $\sigma_y^D \approx \sigma_y^H \approx \sigma_y$, since we are now disregarding any softening effects in the dry versus hydrated states of the matrix. The main change would be in t_4 (hydrated state) and hence t_5 (post-hydrated state) as well. The following analytical equation defines the value of strain at t_4 :

$$\epsilon_4 = \frac{E_M V_M (\epsilon_c + \epsilon_s)}{E_M V_M + E_F V_F} \quad (8)$$

Here, ϵ_s is the additional strain that reflects the amount of swelling occurring in the hydrated matrix, and hence accounts for the expansion of the matrix due to hydration, contributing to the overall deformation response. In this way, ϵ_4 accommodates for the combined effect of imposed plastic strain (ϵ_c) and swelling within the matrix at t_4 , and it enables a comprehensive analysis of the interplay between mechanical deformation and hydration-induced swelling.

To determine the analytical location of stress in the matrix at t_4 (σ_4^M), we can use the following equation:

$$\sigma_4^M = E_M (\epsilon_4 - \epsilon_c - \epsilon_s) \quad (9)$$

On substituting Eq. (8) in Eq. (9), we get:

$$\sigma_4^M = -\frac{E_M E_F V_F (\epsilon_c + \epsilon_s)}{E_M V_M + E_F V_F} \quad (10)$$

It is important to note here that the impact of swelling becomes evident only if the matrix has undergone plastic deformation. This is due to the fact that for small deformations, as per Hooke's law, swelling results in a purely elastic effect, causing the "swollen" matrix to revert to

its initial configuration at time t_5 (or $\epsilon_5 = \epsilon_3$). The critical value of swelling-induced strain ($\epsilon_s = \epsilon_{sT}^c$) when the matrix deforms plastically under tension can be determined by equating σ_4^M from Eq. (10) with the yield stress value of matrix during compression ($-\sigma_y$), and then rearranging the equation accordingly to get:

$$\epsilon_{sT}^c = \frac{\sigma_y(E_M V_M + E_F V_F)}{E_M E_F V_F} - \epsilon_c \quad (11)$$

To examine how swelling affects the final configuration, we must understand its influence on the final plastic strain value ($\epsilon'_c = \epsilon'_{c-sT}$), which is governed by the following constitutive equation:

$$\epsilon'_{c-sT} = \epsilon_c - (\epsilon_s - \epsilon_{sT}^c) \quad (12)$$

On substituting Eq. (11) in Eq. (12), and simplifying, we get:

$$\epsilon'_{c-sT} = \frac{\sigma_y(E_M V_M + E_F V_F)}{E_M E_F V_F} - \epsilon_s \quad (13)$$

Eq. (13) shows that an increase in ϵ_s causes the value of ϵ'_{c-sT} to decrease, which results in a higher degree of recovery, hence making swelling a favorable influence under tensile loading.

The similar analysis can be conducted under uniaxial compression loading, where the key alteration involves equating σ_4^M from Eq. (10) with the yield stress value of the matrix during tension ($+\sigma_y$), to determine the critical value of swelling-induced strain ($\epsilon_s = \epsilon_{sC}^c$), leading to the modified equation:

$$\epsilon_{sC}^c = -\frac{\sigma_y(E_M V_M + E_F V_F)}{E_M E_F V_F} - \epsilon_c \quad (14)$$

Notice that this Eq. (14) is the same as Eq. (11), except for the change in sign of the first term on the right-hand side. On re-formulating the constitutive equation defined in Eq. (12) to see the effect of swelling after compression loading, we find that the new final plastic strain value ($\epsilon'_c = \epsilon'_{c-sC}$) is given by:

$$\epsilon'_{c-sC} = -\frac{\sigma_y(E_M V_M + E_F V_F)}{E_M E_F V_F} - \epsilon_s \quad (15)$$

According to Eq. (15), swelling has an undesirable effect under compression loading since an increase in the magnitude of ϵ_s results in an increase in the value of ϵ'_{c-sC} , thereby lowering the degree of recovery. Hence, from the analysis of MM model-2, we can conclude that swelling benefits shape recovery only when the plastic deformation in the matrix is caused from uniaxial tensile loading and may lead to a detrimental outcome in cases of compression loading.

2.3. MM model-3 (Softening and swelling)

Now that we better understand the hydration influences individually in terms of softening (drop in Young's modulus and yield stress of the matrix) and swelling (strain-induced expansion of the matrix), let us look at their combined effect during hydration. Under uniaxial tensile testing, the MM model-3 will follow the same path as earlier models for positions at times t_1 – t_3 . However, when MM model-3 is subjected to hydration at time t_4 , we start to see the combined impact of swelling and softening of the matrix. In the analysis of MM model-1, we calculated a value for strain (ϵ_4) at t_4 (Fig. 5a shows the previous location of t_4 corresponding to MM model-1 at t_4^*) as shown in Eq. (3), which we now need to modify to account for swelling (ϵ_s). The updated value of strain, $\epsilon'_4 = (\epsilon_4 - \epsilon_s)$ at t_4 , will also affect the value of ϵ'_c (new value is represented with ϵ'_c) as shown in Eq. (18):

$$\epsilon'_c = \frac{\sigma_y^H + E_M^H(\epsilon_4 - \epsilon_s)}{E_M^H} \quad (18)$$

The combined influence of softening and swelling can be studied analytically by comparing Eq. (18) to Eq. (5). The analysis of MM model-

2 revealed that the impact of swelling strain (ϵ_s) can have either a desirable effect (increased recovery rate) or an undesirable effect (reduced recovery rate), depending on whether the model is initially subjected to tension or compression, respectively. A similar impact is also observed in the analysis of MM model-3, as demonstrated by the schematic graphs shown in Fig. 5(a and b). When $\epsilon_s = \epsilon_{sT}^c$, the updated value of ϵ'_4 shifts t_4 closer to the initial zero strain value at t_1 , as the composite undergoes hydration, as illustrated in Fig. 5a. This is because, at t_3 , the matrix undergoes compression while the fibers are under tension. As a result, swelling of the matrix causes it to expand and enter tension, hence assisting in the compression of the fibers and thereby enabling the MM model-3 to contract back to its initial state. Consequently, after drying, this shift has a desirable impact on the strain value (ϵ'_5), which can be calculated using Eq. (19).

$$\epsilon'_5 = \frac{E_M^D V_M \epsilon_c''}{E_M^D V_M + E_F V_F} \quad (19)$$

Conversely, when $\epsilon_s = \epsilon_{sC}^c$, the updated value of ϵ'_4 shifts t_4 farther away from the initial zero strain value at t_1 , as the composite undergoes hydration, as illustrated in Fig. 5b. This occurs because, during initial compression loading, at t_3 , the matrix is already under tension while the fibers are compressed. In this scenario, swelling of the matrix exacerbates the compression of the fibers, hence hindering the return of MM model-3 to its initial state. As a result, after drying, this shift has an adverse effect on the strain value (ϵ'_5), resulting in a lower degree of shape recovery.

The recovery strain parameter ($\epsilon'_r = (\epsilon_3 - \epsilon'_5)/\epsilon_3$) can be used to quantify the degree of shape recovery for the MM model-3 and is defined as:

$$\epsilon'_r = 1 - \frac{\left(\frac{\sigma_y^H}{E_M^H}\right) + \left(\frac{\sigma_y^H V_M}{E_F V_F}\right) - \epsilon_s}{(\Delta_M/L_0) - \left(\frac{\sigma_y^D}{E_M^D}\right)} \quad (20)$$

The recovery strain parameter (ϵ'_r), defined in Eq. (20), quantifies the degree of shape recovery by comparing the strain at the deformed equilibrium state (ϵ_3) with the strain after recovery (ϵ'_5). This metric validates the model by demonstrating the efficiency of the hydration-driven recovery process. For instance, when swelling aids recovery, as in tensile loading conditions ($\epsilon_s = \epsilon_{sT}^c$), the parameter ϵ'_r increases, highlighting favorable recovery. Conversely, when swelling hinders recovery, as in compression loading ($\epsilon_s = \epsilon_{sC}^c$), ϵ'_r decreases, reflecting reduced recovery efficiency.

From the juxtaposition and analysis of these MM models, we can conclude that softening in the matrix is an essential contributor to shape recovery. Further, swelling in the matrix is only selectively beneficial and may even be undesirable in some cases. As explained above, the swelling phenomenon is more advantageous during initial tensile loading due to the inherent mechanics of the MM model.

It is important to note that our analysis of MM models-1, 2, and 3 provides valuable insights under idealized 1D conditions with uniaxial stress scenarios. This limited perspective does not encompass the additional complexities of more realistic, multi-axial, inelastic deformation and damage. In practical scenarios involving bending, twisting, and substantial deformation, the movement, rotation, or buckling of fibers may occur, deviating from the ideal straight geometry, as considered in the current models. In such instances, swelling might play a role in straightening out the fibers, potentially contributing to the recovery and healing of local deformations. While our model underscores the significance of matrix softening as a primary driver for shape recovery, it does not fully capture the potential benefits of swelling in more complex, real-world scenarios. This limitation prompts consideration for future investigations into the nuanced interplay of swelling and mechanical behavior, offering a foundation for developing design guidelines for shape memory materials. The following sections illustrate benchmark

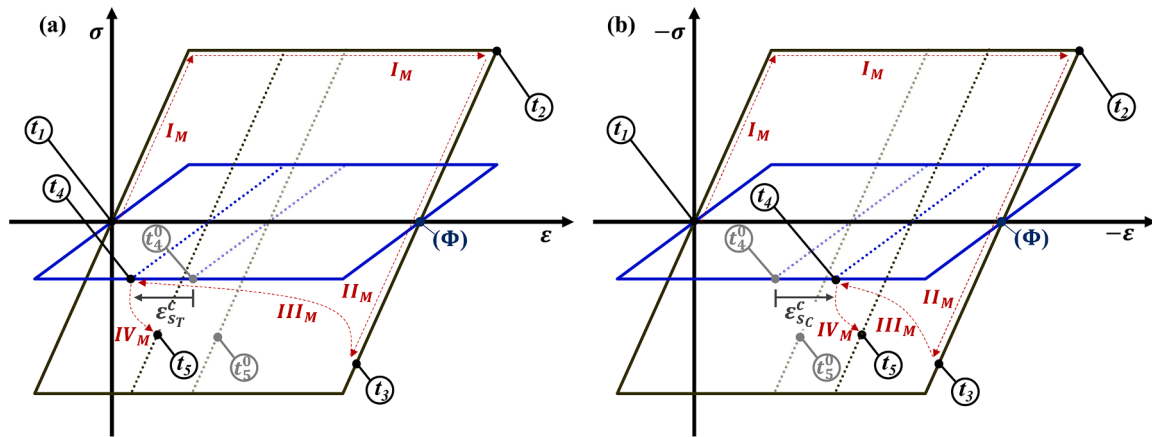


Fig. 5. Response of the Matrix in MM Model-3 under Uniaxial Loading and Hydration. Schematic stress-strain behavior in the dry (black) and hydrated (blue) states of the matrix when it initially undergoes plastic deformation due to (a) tensile loading (swelling here is favorable to shape recovery) (b) compressive loading (swelling here is unfavorable to shape recovery). The time steps (t_i) and Roman numerals (I – IV) used in this figure are the same as those defined in Fig. 4.

models that show the boon and bane of swelling within the matrix under different loading scenarios.

3. Computational models for benchmark testing

3.1. Cross-validation of analytical and FEA models

Before advancing to the benchmark models, the validation of the above analytical findings was done through a two-step process. First, we verified our analytical equations by constructing a MM model of a 2D rectangular matrix-fiber laminate and conducting analyses with commercial FEA software ABAQUS CAE (version 2021), using four-node plane strain (CPE4R) elements to discretize the model. Mesh convergence was performed by refining the element size incrementally until the stress-strain and recovery results showed negligible variation, ensuring independence from the mesh density. The Eqs. (1)–(20) delineated in Section 2, along with the constitutive behaviors of the fiber and matrix as illustrated in Fig. 3, were meticulously tested through this FEA model, with the resulting curves, such as those in Figs. 4(b, c) and 5, showing quantitative agreement with the analytical results, with stress-strain curves and recovery parameters deviating by less than 2%.

Next, we conducted a comparative analysis utilizing a pure bending test setup to determine the optimal number of matrix and fiber layers to design a reduced order 2D shell lay-up FEA composite model to mimic the composition of the feather shaft and is what we refer to as a CFSC model as briefly described in the introduction section. In this setup, the ends of the laminate were kinematically constrained to reference points at each end, and uniform bending moments were induced through quasistatic displacement-controlled loading without introducing shear or axial forces. The laminate model was subjected to flexural bending under these conditions, followed by the release of the load to induce permanent plastic deformation post spring-back. Subsequently, the laminate was exposed to a hydration process for shape recovery, followed by dehydration to remove excess water molecules (see Fig. 6a). Here, hydration was simulated by reducing the matrix properties to hydrated values (E_M^H, σ_y^H) and applying swelling strain as an initial condition, while dehydration reversed these parameters to their dry state values (E_M^D, σ_y^D) and removed the swelling strain. The ratio of the absolute maximum in-plane principal stress (σ_1) to the yield stress of the matrix with zero moisture content (σ_y^D) was employed as a dimensionless parameter to indicate the level of plastic deformation within the model during this process. The same test setup was replicated with the CFSC model that was discretized using four-node doubly curved thin shell (S4R) elements.

The number of total layers was varied according to the $2n+1$ rule, starting with $n = 1$, while maintaining a fixed volume fraction of fibers at 40%. To assess convergence, we used a dimensionless measure called the percentage of recovery ratio (ξ), calculated as the percentage ratio of the final central angle to the initial central angle (180° for a straight line) subtended by the neutral axis of the laminate. The material properties used for both the matrix and fiber were obtained from literature [45] and were chosen to replicate the properties of the amorphous matrix and the crystalline fibers found in keratinous materials inside the cortex of feather shafts. Additionally, we examined the effect of swelling under pure bending by subjecting all simulations to testing with and without considering any swelling associated with the matrix. Validation of the composite shell model was done by comparing the percentage of recovery ratio with the equivalent micromechanical model. The value of ξ showed a perfect match and exhibited convergence trends at 97.6% for models without swelling and 99.7% for models with swelling (see Fig. 6b), both observed at the configuration of 31 layers (consisting of 16 matrix layers and 15 fiber layers), hence confirming its validity at this configuration. Notably, here, swelling was found to play a beneficial role in marginally enhancing the SME when subjected to flexural bending. Subsequently, the validated CFSC model was utilized in devising benchmark testing scenarios involving hollow thin shell cylindrical pipes subjected to individual bending and twisting simulations. These scenarios were designed to demonstrate SME and explore regions where large, localized instabilities and buckling are expected to occur.

3.2. Benchmark models

In these benchmark simulations, hollow thin cylindrical pipes (with thickness-to-diameter ratio of 0.1 and a diameter-to-length ratio of 0.05) made from CFSC underwent the following well-defined stages. Initially, the pipes were in their undeformed configuration, with a straight central angle of 180° . Subsequently, the pipes were subjected to quasistatic displacement-controlled loading to induce deformation, primarily resulting from buckling instabilities due to bending (Fig. 7a) and twisting (Fig. 7b). The FEA analysis captured the progressive accumulation of plastic strain within the pipes, with results visually depicted through contour plots at each test stage, as illustrated in Fig. 7. During the unloading phase, the pipes underwent spring-back owing to elastic rebound until they reached a state of permanent deformation at equilibrium. Following this, a hydration process was introduced, triggering SME, which enabled the pipes to gradually recover their original shape. Finally, the pipes were dehydrated, leading to a slight spring-forward and effectively locking in the recovered shape. These benchmark tests were again conducted and analyzed with and without considering

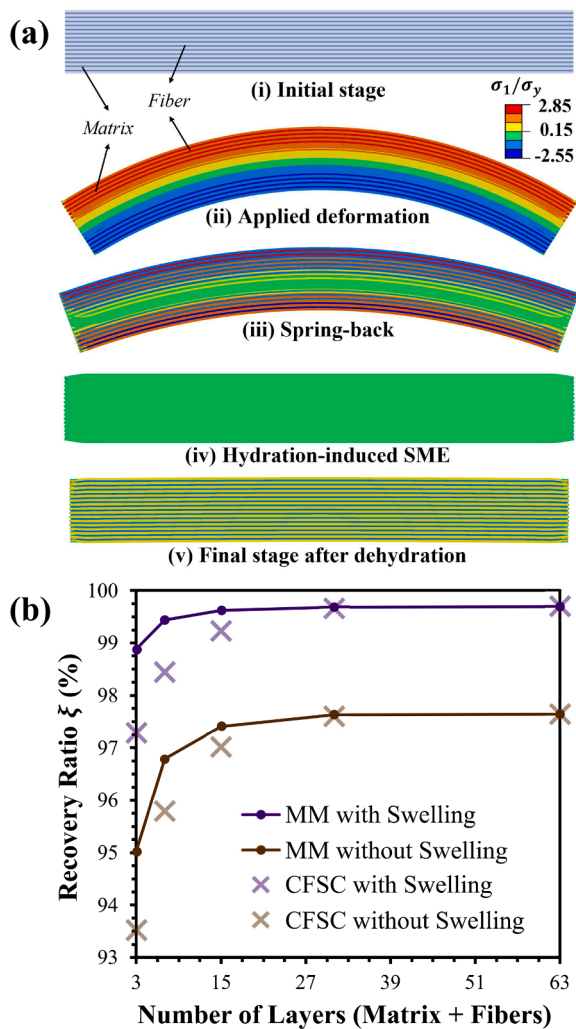


Fig. 6. Finite Element Simulations of the Shape Recovery Process of the MM and CFSC Models under Flexural Bending. (a) The MM laminate model is loaded under pure flexural bending causing it to deform plastically with a certain amount of spring-back, followed by hydration to trigger and facilitate shape recovery and finally dehydrated to lock in the recovered shape after a slight spring-forward. (b) Comparison of the MM model and a reduced order CFSC model to study convergence analysis with an increase in the number of layers. Both the MM model and the CFSC models are also simulated with and without any swelling associated with the matrix, and we see that under flexural bending, swelling is favorable.

swelling associated with the matrix, enabling a comprehensive understanding of the influence of swelling under different loading scenarios.

The value of ξ (here, the ratio is calculated using the angles subtended by the neutral axis of the hollow pipes in the initial and final configurations) was once again used as a quantitative measure of comparison to assess the influence of swelling during bending versus twisting. The results revealed that during bending, the pipes with swelling within the matrix displayed a higher rate of shape memory effect ($\xi = 97.8\%$) compared to those without swelling ($\xi = 96.3\%$). However, in the case of twisting, a contrasting behavior emerged, wherein the presence of swelling proved to be disadvantageous. Specifically, the model without any swelling exhibited a higher rate of shape memory effect ($\xi = 99.4\%$) compared to the model with swelling ($\xi = 98.1\%$). These findings underscore the nuanced interplay between swelling and the shape memory effect, which varies under distinct loading conditions, providing valuable insights into the material response. Hence, further strengthening our claim that swelling within

the matrix is only conditionally favorable to the overall SME of the CFSC model. Furthermore, it is worth emphasizing that while swelling does offer a slight advantage in SME, the primary driver of SME is the softening component of the matrix. Consequently, for future design and bioinspired modeling endeavors, the complex characteristics of swelling may not require detailed modeling and could potentially be overlooked.

3.3. Exploring the potential of these design principles and future works

To expand on its potential future applications, it is important to highlight that the CFSC model exhibits high flexibility, allowing for precise programming of shape recovery by systematically controlling the volume fraction of its fibers. This tunability renders the composite highly suitable for a diverse array of engineering applications. To illustrate the extent of its tunability, we present a flower design that emulates the controlled "blooming" and "wilting" of petals. We model and analyze the flower design, where the base and each petal are represented as rigid bodies, while the CFSC serves as a flexible hinge that connects the petals to the base (see Fig. 8a).

The simulation process involves four distinct stages, as depicted in Fig. 8a. In the initial stage, deformation is induced in the CFSC, simulating the controlled "blooming" of petals under displacement-controlled loading. Subsequently, in the second stage, the loading is released, and the flower undergoes spring-back until it reaches a state of permanent plastic deformation at equilibrium. It is important to emphasize that the applied load in the first stage is carefully tweaked to achieve a consistent configuration of permanent plastic deformation after spring-back, as shown in Fig. 8b. Moving on to the third stage, the flower undergoes hydration, initiating the process of shape recovery. Finally, in the fourth stage, the flower is dried, resulting in the observation of a slight spring-forward and locking in the recovered shape. Throughout these simulations, various volume fractions of fibers are employed, ranging from 1% to 25%. The degree of shape recovery at the hydration and drying stages is then individually determined using the percentage of recovery ratio ξ_i parameter (similar to ξ used earlier). Here, $\xi_i = \xi_H$ is the recovery ratio of the CFSC under 100% hydration, and $\xi_i = \xi_D$ is the recovery ratio of the CFSC at the final stage after dehydration.

Once again, these simulations are examined under two conditions: one with swelling incorporated within the matrix and the other without such alterations. As anticipated based on prior observations, the models with swelling performed slightly better under bending, as shown in Fig. 8b. However, it is important to acknowledge that this advantage is contingent upon the specific loading scenarios. In situations where we modify the loading conditions, we must exercise caution, as the favorability of swelling becomes conditional and may not consistently yield better outcomes. Moreover, while swelling might offer advantages under specific circumstances, its impact on overall SME remains relatively minor.

We can extend our exploration beyond the specified range of fiber volume fractions considered in this study to attain theoretical values of 100% degree of shape recovery. However, achieving a constant state of permanent plastic deformation requires careful consideration of the spring-back effect exhibited by the CFSC after load release. To account for the spring-back, as we increase the fiber volume fraction, we must also exponentially increase the applied deformation, as shown in Fig. 8b. Furthermore, it is worth noting that while we have duplicated the material properties observed in feather shafts for this study, the proposed analytical framework can be adapted to encompass various other simple materials. This extended applicability opens up additional levels of tunability and versatility that are guided by the design principles adapted from the working of feather shafts in avian birds.

4. Conclusions

Insights into the keratinous structure within the feather cortex of birds of prey, offer a promising foundation for designing new classes of

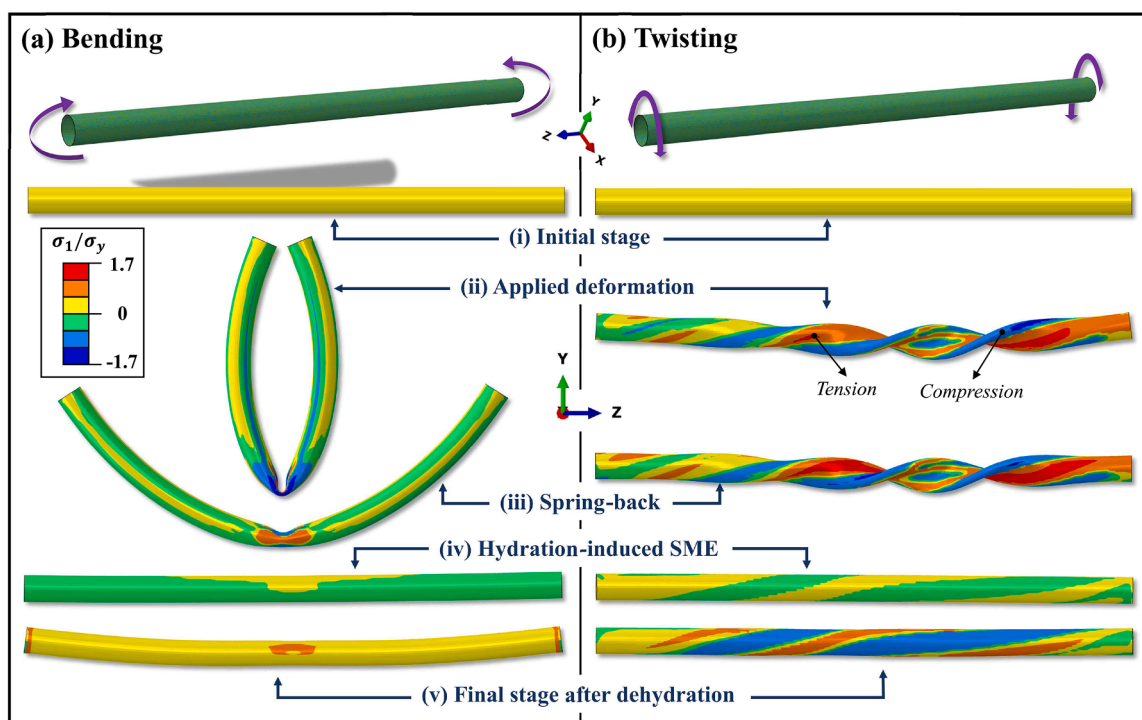


Fig. 7. Finite Element Simulations of the Shape Recovery Process of the CFSC as a Hollow Thin Cylindrical Pipe. The CFSC pipe is simulated as a FEA model that is deformed under (a) bending versus (b) twisting. Both of these cases are simulated with and without any swelling associated with the matrix, and we see that under flexural bending, swelling is favorable; however, the model without swelling displayed a higher degree of shape recovery in the twisting scenario. Here, only the simulations that performed best (without swelling for bending and with swelling for twisting) are illustrated.

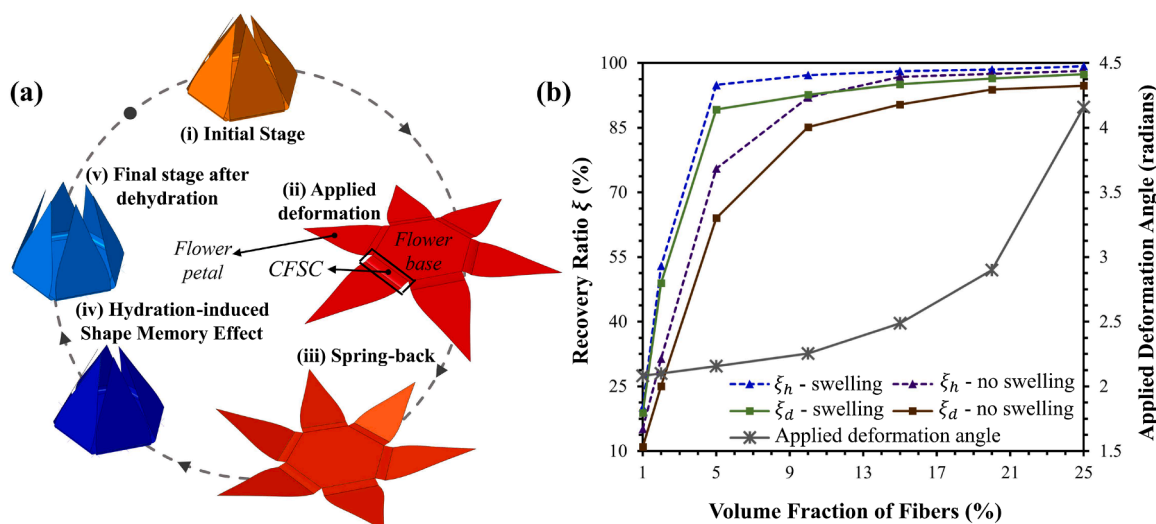


Fig. 8. Demonstration of Potential Application of the CFSC via FEA Simulations Illustrating the Blooming and Wilting of a Flower. (a) The CFSC is modeled as a composite that acts as a hinged link that connects the flower petals to the flower base which are both modeled as rigid bodies. Here, the blooming of the flower is considered as deformation, while wilting is representative of the shape recovery process. (b) The flower model is simulated to demonstrate the capacity of the CFSC to custom-tune its degree of shape recovery during wilting by varying the volume fraction of the fibers. To achieve a consistent configuration of permanent plastic deformation after spring-back, all models are subjected to tailored applied deformation as shown by the solid grey line. Percentage of recovery ratio is plotted at both the hydration (hyphenated) stage and the final stage post dehydration (solid) to show the level of spring-forward after drying. Again, all models are simulated with and without any swelling associated with the matrix.

materials that can exhibit shape memory behavior, without the need for inherently active shape memory components. This paper shows that the hydration-induced softening of the matrix emerges as a primary mechanism that enables the shape memory effect. The hydration-induced softening mechanism we identified in keratinous structures provides a bioinspired framework for the development of new classes of shape

memory materials. These materials do not rely on inherently active shape memory components but instead exploit hydration as a tunable parameter to achieve shape recovery. This approach introduces a versatile and simplified design paradigm, which expands the applicability of shape memory systems and bridges the gap between natural and synthetic materials.

Although swelling shows some favorable results, its contribution is marginal compared to the effect of matrix softening when considering only uniaxial deformation. Moreover, swelling only demonstrated conditional favorability. For instance, hydration-induced swelling promotes shape recovery under bending conditions but may yield undesirable results during twist-loading scenarios. However, it is important to note that the scope of this analysis is confined to a simple uniaxial case, specifically considering a composite material under uniaxial stress conditions where the load is applied only parallel to the fiber orientation. In contrast, real feathers exhibit a highly hierarchical structure with anisotropic mechanical properties and are subjected to complex, multi-axial loading scenarios, including bending, twisting, and shear. Future studies could expand on the current work by incorporating multi-axial loading scenarios, such as bending, twisting, and shear, which require transitioning to two-dimensional or three-dimensional modeling frameworks. This would involve the implementation of 3D stress tensors and constitutive equations specifically designed to capture anisotropic and heterogeneous mechanical properties of keratinous materials. Further analysis is also required to explore the role of swelling under these more intricate loading conditions. While this lies beyond the scope of the current work, these directions offer exciting opportunities for future exploration.

The design principles outlined here can be extended to exhibit flexibility and tunability in achieving different degrees of shape recovery by systematically controlling the volume fraction of the fibers. Further, the inherent versatility in material selection allows for incorporating constituent materials without innate shape memory properties, hence broadening the range of possibilities to include passive and simpler elements. Such tunability in these systems can be enhanced through the application of machine learning models, as demonstrated in previous works [66–69]. Machine learning techniques can optimize material selection, geometrical configurations, and recovery behaviors, advancing the design principles toward achieving mechanical intelligence, where materials adapt passively to environmental changes [70]. An important point to highlight in this paper is that we have examined the softening of the matrix as a combined effect resulting from a simultaneous reduction in both strength and stiffness. This approach was chosen to emulate the natural functioning observed in the calamus section of feather shafts. Future work can focus on physically modeling and experimentally testing some of these feather shaft-inspired design principles, while also exploring machine learning as a tool for guiding and accelerating the design process.

CRediT authorship contribution statement

Phani Saketh Dasika: Writing – review & editing, Writing – original draft, Visualization, Validation, Software, Investigation, Formal analysis. **Yunlan Zhang:** Writing – original draft, Validation, Investigation, Formal analysis, Conceptualization. **Tarah N. Sullivan:** Investigation, Formal analysis, Conceptualization. **Sheron Tavares:** Data curation, Investigation, Methodology, Visualization. **Marc A. Meyers:** Writing – original draft, Supervision, Project administration, Funding acquisition, Formal analysis, Conceptualization. **Pablo D. Zavattieri:** Writing – review & editing, Writing – original draft, Supervision, Project administration, Methodology, Investigation, Funding acquisition, Formal analysis, Conceptualization.

Declaration of competing interest

The authors declare that they have no known competing financial interests or personal relationships that could have appeared to influence the work reported in this paper.

Acknowledgments

This work was part of the AFOSR MURI (AFOSR-FA9550-15-1-

0009). Y.Z. and P.D.Z. would like to acknowledge partial support by the National Science Foundation through the GOALI award CMMI-1538898.

Supplementary materials

Supplementary material associated with this article can be found, in the online version, at doi:10.1016/j.actbio.2025.02.017.

References

- [1] L. Sun, W.M. Huang, Z. Ding, Y. Zhao, C.C. Wang, H. Purnawali, C. Tang, Stimulus-responsive shape memory materials: a review, *Mater. Des.* 33 (2012) 577–640.
- [2] M. Mrinalini, S. Prasanthkumar, Recent advances on stimuli-responsive smart materials and their applications, *ChemPlusChem* 84 (8) (2019) 1103–1121.
- [3] D. Roy, J.N. Cambre, B.S. Sumerlin, Future perspectives and recent advances in stimuli-responsive materials, *Prog. Polym. Sci.* 35 (1–2) (2010) 278–301.
- [4] Q. Zheng, C. Xu, Z. Jiang, M. Zhu, C. Chen, F. Fu, Smart actuators based on external stimulus response, *Front. Chem.* 9 (2021) 650358.
- [5] X. Zhang, L. Chen, K.H. Lim, S. Gonuguntla, K.W. Lim, D. Pranantyo, W.P. Yong, W. J.T. Yam, Z. Low, W.J. Teo, H.P. Nien, Q.W. Loh, S. Soh, The pathway to intelligence: using stimuli-responsive materials as building blocks for constructing smart and functional systems, *Adv. Mater.* 31 (11) (2019) 1804540.
- [6] I.L. Sokolov, V.R. Cherkasov, A.A. Tregubov, S.R. Buiuciu, M.P. Nikitin, Smart materials on the way to theranostic nanorobots: molecular machines and nanomotors, advanced biosensors, and intelligent vehicles for drug delivery, *Biochim. Biophys. Acta (BBA) Gen. Subj.* 1861 (6) (2017) 1530–1544.
- [7] Y. Zhao, K. Thorkelsson, A.J. Mastroianni, T. Schilling, J.M. Luther, B.J. Rancatore, K. Matsunaga, H. Jinnai, Y. Wu, D. Poulsen, J.M.J. Fréchet, A.P. Alivisatos, T. Xu, Small-molecule-directed nanoparticle assembly towards stimuli-responsive nanocomposites, *Nat. Mater.* 8 (12) (2009) 979–985.
- [8] O. Onaca, R. Enea, D.W. Hughes, W. Meier, Stimuli-responsive polymersomes as nanocarriers for drug and gene delivery, *Macromol. Biosci.* 9 (2) (2009) 129–139.
- [9] D. Schmaljohann, Thermo- and pH-responsive polymers in drug delivery, *Adv. Drug Deliv. Rev.* 58 (15) (2006) 1655–1670.
- [10] W.T. Huck, Responsive polymers for nanoscale actuation, *Mater. Today* 11 (7–8) (2008) 24–32.
- [11] M.A.C. Stuart, W.T. Huck, J. Genzer, M. Müller, C. Ober, M. Stamm, G. B. Sukhorukov, I. Szleifer, V.V. Tsukruk, M. Urban, F. Winnik, S. Zauscher, I. Luzinov, S. Minko, Emerging applications of stimuli-responsive polymer materials, *Nat. Mater.* 9 (2) (2010) 101–113.
- [12] S. Miyazaki, Y.Q. Fu, W.M. Huang, *Thin Film Shape Memory Alloys: Fundamentals and Device Applications*, Cambridge University Press, 2009.
- [13] A.J. Thornton, E. Alsberg, M. Albertelli, D.J. Mooney, Shape-defining scaffolds for minimally invasive tissue engineering, *Transplantation* 77 (12) (2004) 1798–1803.
- [14] L. Hsu, C. Weder, S.J. Rowan, Stimuli-responsive, mechanically-adaptive polymer nanocomposites, *J. Mater. Chem.* 21 (9) (2011) 2812–2822.
- [15] B. Zhang, J.E. DeBartolo, J. Song, Shape recovery with concomitant mechanical strengthening of amphiphilic shape memory polymers in warm water, *ACS Appl. Mater. Interfaces* 9 (5) (2017) 4450–4456.
- [16] W.M. Huang, Z. Ding, C.C. Wang, J. Wei, Y. Zhao, H. Purnawali, Shape memory materials, *Mater. Today* 13 (7–8) (2010) 54–61.
- [17] A. Lendlein, S. Kelch, Shape-memory polymers, *Angew. Chem. Int. Ed.* 41 (12) (2002) 2034–2057.
- [18] Y. Wu, Y. Lin, Y. Zhou, F. Zuo, Z. Zheng, X. Ding, Light-induced shape memory polymer materials, *Prog. Chem.* 2004 (10) (2012).
- [19] Y. Liu, H. Lv, X. Lan, J. Leng, S. Du, Review of electro-active shape-memory polymer composite, *Compos. Sci. Technol.* 69 (13) (2009) 2064–2068.
- [20] S.J. van Vilsteren, H. Yarmand, S. Ghodrati, Review of magnetic shape memory polymers and magnetic soft materials, *Magnetochemistry* 7 (9) (2021) 123.
- [21] W.M. Huang, B. Yang, L. An, C. Li, Y.S. Chan, Water-driven programmable polyurethane shape memory polymer: demonstration and mechanism, *Appl. Phys. Lett.* 86 (11) (2005) 114105.
- [22] T. Tadaki, K. Otsuka, K. Shimizu, Shape memory alloys, *Annu. Rev. Mater. Sci.* 18 (1) (1988) 25–45.
- [23] M. Behl, A. Lendlein, Shape-memory polymers, *Mater. Today* 10 (4) (2007) 20–28.
- [24] L. Sun, W.M. Huang, Mechanisms of the multi-shape memory effect and temperature memory effect in shape memory polymers, *Soft Matter* 6 (18) (2010) 4403–4406.
- [25] N. Choudhary, D. Kaur, Shape memory alloy thin films and heterostructures for MEMS applications: a review, *Sens. Actuators A Phys.* 242 (2016) 162–181.
- [26] I. Stachiv, E. Alarcon, M. Lamac, Shape memory alloys and polymers for MEMS/NEMS applications: review on recent findings and challenges in design, preparation, and characterization, *Metals* 11 (3) (2021) 415.
- [27] J. Mohd Jani, M. Leary, A. Subic, Designing shape memory alloy linear actuators: a review, *J. Intell. Mater. Syst. Struct.* 28 (13) (2017) 1699–1718.
- [28] A. Lendlein, O.E. Gould, Reprogrammable recovery and actuation behaviour of shape-memory polymers, *Nat. Rev. Mater.* 4 (2) (2019) 116–133.
- [29] G. Costanza, M.E. Tata, Shape memory alloys for aerospace, recent developments, and new applications: a short review, *Materials* 13 (8) (2020) 1856.
- [30] Y. Liu, H. Du, L. Liu, J. Leng, Shape memory polymers and their composites in aerospace applications: a review, *Smart Mater. Struct.* 23 (2) (2014) 023001.
- [31] J.W. Sohn, G.W. Kim, S.B. Choi, A state-of-the-art review on robots and medical devices using smart fluids and shape memory alloys, *Appl. Sci.* 8 (10) (2018) 1928.

- [32] J. Delaey, P. Dubruel, S. Van Vlierberghe, Shape-memory polymers for biomedical applications, *Adv. Funct. Mater.* 30 (44) (2020) 1909047.
- [33] L. Janke, C. Czaderski, M. Motavalli, J. Ruth, Applications of shape memory alloys in civil engineering structures—overview, limits and new ideas, *Mater. Struct.* 38 (2005) 578–592.
- [34] M. Elahinia, N.S. Moghaddam, M.T. Andani, A. Amerinatanzi, B.A. Bimber, R. F. Hamilton, Fabrication of NiTi through additive manufacturing: a review, *Prog. Mater. Sci.* 83 (2016) 630–663.
- [35] Y. Zhang, M. Velay-Lizancos, D. Restrepo, N.D. Mankame, P.D. Zavattieri, Architected material analogs for shape memory alloys, *Matter* 4 (6) (2021) 1990–2012.
- [36] Q. Ge, A.H. Sakhaei, H. Lee, C.K. Dunn, N.X. Fang, M.L. Dunn, Multimaterial 4D printing with tailorable shape memory polymers, *Sci. Rep.* 6 (1) (2016) 31110.
- [37] C.J. Pennycuik, *Modelling the Flying Bird*, Elsevier, 2008.
- [38] J.E. Loye, M. Zuk, *Bird-parasite interactions: ecology, evolution and behaviour. Bird-Parasite Interactions: Ecology, Evolution and Behaviour*, Oxford University Press, 1991. Ornithology Series, 2.
- [39] E.H. Burt Jr, J.M. Ichida, Occurrence of feather-degrading bacilli in the plumage of birds, *Auk* 116 (2) (1999) 364–372.
- [40] M.M. Muza, E.H. Burt, J.M. Ichida, Distribution of bacteria on feathers of some eastern North American birds, *Wilson Bull.* 112 (3) (2000) 432–435.
- [41] D. Praveenkumar, A. Vinothkumar, G. Saravanan, M. Selvakumar, A. S. Vijayakumar, P. Kolanchinathan, S. Kamalakkannan, S. Achiraman, Symbiotic microbes play a role more important than preen gland in avian pheromone production—a review, *Avian Biol. Res.* 16 (1) (2023) 32–41.
- [42] S.E. Bush, D.H. Clayton, Anti-parasite behaviour of birds, *Philos. Trans. R. Soc. B Biol. Sci.* 373 (1751) (2018) 20170196.
- [43] W.D. Yu, Z. Du, H. Liu, W. Yu, Fractal structure and hydration-driven shape memory of duck down in the dry–wet state, *Text. Res. J.* 92 (9–10) (2022) 1444–1453.
- [44] Z.Q. Liu, D. Jiao, Z.F. Zhang, Remarkable shape memory effect of a natural biopolymer in aqueous environment, *Biomaterials* 65 (2015) 13–21.
- [45] T.N. Sullivan, Y. Zhang, P.D. Zavattieri, M.A. Meyers, Hydration-induced shape and strength recovery of the feather, *Adv. Funct. Mater.* 28 (30) (2018) 1801250.
- [46] F.B. Gill, *Ornithology*, Macmillan, 1995.
- [47] T. Bachmann, J. Emmerlich, W. Baumgartner, J.M. Schneider, H. Wagner, Flexural stiffness of feather shafts: geometry rules over material properties, *J. Exp. Biol.* 215 (3) (2012) 405–415.
- [48] B. Wang, W. Yang, J. McKittrick, M.A. Meyers, Keratin: structure, mechanical properties, occurrence in biological organisms, and efforts at bioinspiration, *Prog. Mater. Sci.* 76 (2016) 229–318.
- [49] B. Wang, M.A. Meyers, Light like a feather: a fibrous natural composite with a shape changing from round to square, *Adv. Sci.* 4 (3) (2017) 1600360.
- [50] T. Lingham-Soliar, R.H. Bonser, J. Wesley-Smith, Selective biodegradation of keratin matrix in feather rachis reveals classic bioengineering, *Proc. R. Soc. B Biol. Sci.* 277 (1685) (2010) 1161–1168.
- [51] J. McKittrick, P.Y. Chen, S.G. Bodde, W. Yang, E.E. Novitskaya, M.A. Meyers, The structure, functions, and mechanical properties of keratin, *JOM* 64 (2012) 449–468.
- [52] Fraser, R.D.B., MacRae, T.P., & Rogers, G.E. (1972). Keratins: their composition, structure and biosynthesis.
- [53] B. Wang, M.A. Meyers, Seagull feather shaft: correlation between structure and mechanical response, *Acta Biomater.* 48 (2017) 270–288.
- [54] Z.Q. Liu, D. Jiao, Z.Y. Weng, Z.F. Zhang, Water-assisted self-healing and property recovery in a natural dermal armor of pangolin scales, *J. Mech. Behav. Biomed. Mater.* 56 (2016) 14–22.
- [55] W. Huang, A. Zaheri, W. Yang, D. Kisailus, R.O. Ritchie, H. Espinosa, J. McKittrick, How water can affect keratin: hydration-driven recovery of bighorn sheep (*Ovis canadensis*) horns, *Adv. Funct. Mater.* 29 (27) (2019) 1901077.
- [56] X. Xiao, J. Hu, X. Gui, J. Lu, H. Luo, Is biopolymer hair a multi-responsive smart material? *Polym. Chem.* 8 (1) (2017) 283–294.
- [57] C.O. Correia, S.G. Caridade, J.F. Mano, Chitosan membranes exhibiting shape memory capability by the action of controlled hydration, *Polymers* 6 (4) (2014) 1178–1186.
- [58] J. Hu, Y. Zhu, Spider silk: a smart biopolymer with water switchable shape memory effects—unraveling the mystery of supercontraction, *Res. J. Text. Appar.* (2013).
- [59] B.S. Lazarus, C. Chadha, A. Velasco-Hogan, J.D. Barbosa, I. Jasiuk, M.A. Meyers, Engineering with keratin: a functional material and a source of bioinspiration, *iScience* 24 (8) (2021) 102798.
- [60] H. Quan, D. Kisailus, M.A. Meyers, Hydration-induced reversible deformation of biological materials, *Nat. Rev. Mater.* 6 (3) (2021) 264–283.
- [61] Zhang, Y. (2019). *Stress-and temperature-induced phase transforming architected materials with multistable elements* (Doctoral Dissertation, Purdue University).
- [62] R.D. Fraser, T.P. MacRae, Molecular structure and mechanical properties of keratins, in: *Proceedings of the Symposia of the Society for Experimental Biology* 34, 1980, pp. 211–246.
- [63] A. Kitchener, J.F. Vincent, Composite theory and the effect of water on the stiffness of horn keratin, *J. Mater. Sci.* 22 (1987) 1385–1389.
- [64] M. Feughelman, *Mechanical Properties and Structure of Alpha-Keratin Fibres: Wool, Human Hair and Related Fibres*, UNSW Press, 1997.
- [65] M. Feughelman, M.S. Robinson, The relationship between some mechanical properties of single wool fibers and relative humidity, *Text. Res. J.* 37 (6) (1967) 441–446.
- [66] K. Hector, P.S. Dasika, J.J. Rimoli, P. Zavattieri, Decoupling stiffness and peak moment via hierarchical snapping structures designed with machine learning, *Mater. Des.* 244 (2024) 113189.
- [67] H. Jin, E. Zhang, H.D. Espinosa, Recent advances and applications of machine learning in experimental solid mechanics: a review, *Appl. Mech. Rev.* 75 (6) (2023) 061001.
- [68] J.E. Gubernatis, T. Lookman, Machine learning in materials design and discovery: examples from the present and suggestions for the future, *Phys. Rev. Mater.* 2 (12) (2018) 120301.
- [69] X. Zheng, X. Zhang, T.T. Chen, I. Watanabe, Deep learning in mechanical metamaterials: from prediction and generation to inverse design, *Adv. Mater.* 35 (45) (2023) 2302530.
- [70] A. Khareshi, H. Rajabi, Mechanical intelligence (MI): a bioinspired concept for transforming engineering design, *Adv. Sci.* 9 (32) (2022) 2203783.